

Optical detection of single sub-15 nm objects using elastic scattering strong coupling

MohammadReza Aghdaee and Oluwafemi S. Ojambati*

Faculty of Science and Technology, MESA+ Institute for Nanotechnology,
University of Twente, Enschede, 7522 NB, The Netherlands.

*Corresponding author: o.s.ojambati@utwente.nl

Abstract

Metallic nano-objects play crucial roles in diverse fields, including biomedical imaging, nanomedicine, spectroscopy, and photocatalysis. Nano-objects with sizes that are less than 15 nm exhibit extremely low light scattering cross-sections, posing a significant challenge for optical detection. A possible approach to enhance the optical detection is to exploit nonlinearity of strong coupling regime, especially for elastic light scattering, which is universal to all objects. However, there is still no observation of the strong coupling of elastic light scattering from nano-objects. Here, we demonstrate the strong coupling of elastic light scattering in self-assembled plasmonic nanocavities formed between a gold (Au) nanoprobe and an Au film. We employ this technique to detect individual objects with diameters down to 1.8 nm inside the nanocavity. The resonant mode of the nano-object on the Au film strongly couples with the nanocavity mode, revealing anti-crossing scattering modes under dark-field spectroscopy. The experimental result agrees well with numerical calculations, which we use to extend this technique to other metals, including silver, copper, and aluminum. Furthermore, our results show that the scattering cross-section ratio of the nano-object scales with the electric field to the fourth power, similar to surface-enhanced Raman spectroscopy. This work establishes a new possibility of elastic strong coupling and demonstrates its applicability for observing small, non-fluorescent, Raman inactive sub-15 nm objects, complementary to existing microscopes.

Keywords: Strong coupling; light scattering; plasmonic nanocavity; metallic nanoparticle; nanoscale detection.

1 Main

Nano-scale objects are ubiquitous in physical, chemical, and biological systems [1]. Small metallic nanoparticles, in particular, are widely applied in various fields, including catalysis [2], spectroscopy [3, 4] and sensing [5], biomedicine for drug delivery [6], in biomedical imaging for contrast enhancement [7, 8], and electronics to create transistors and logic circuits [9]. Metallic nanoparticles also have detrimental effects as environmental pollutants [10], defects in integrated circuits [11], and are possibly bio-toxic, resulting in cancer [12]. It is, therefore, of broad interest to investigate and characterize nanoparticles.

Despite their importance, it is challenging to optically detect and image nanoparticles much smaller than the wavelength of visible light. This challenge is due to the scattering cross-section that scales $\sigma_{\text{sca}} \propto R^6$, where R is the radius of the nanoparticle, following Mie theory [13]. This nonlinear scaling implies that the scattered intensity by a 10 nm nanoparticle is 10^6 times less than a 100 nm nanoparticle. As a result, far-field optical techniques can directly detect the elastic light scattering by individual larger nanoparticles (~ 100 nm) [14]. However, a single smaller object (*e.g.*, diameter < 15 nm), which we refer to as “nano-object” henceforth, scatters light so weakly that it is not observed on a standard optical microscope. In addition, many nano-objects do not have fluorescence and phosphorescence due to the absence of an electronic transition in the visible region. Moreover, the nano-objects do not have distinct vibrational modes that can be detected using Raman or infrared spectroscopy. The weak elastic light scattering and extinction are the dominant optical signals from the nano-objects.

Existing optical techniques use different approaches to obtain signals from the nano-objects [15]. Single-molecule fluorescence-based techniques require fluorescent markers, which photobleach and have a limited photon count [16–18]. Scattering-based techniques avoid these limitations and increase scattering contrast using interference [19–21], a scanning probe to collect nearfield [22], and intensity modulation [23]. The drawback of these techniques is mainly the low signal-to-noise ratio of the measured scattered light of small objects, and/or they have a slow scan speed. An alternative approach is photothermal microscopy, where a heated nano-object changes the refractive index of an embedding medium while a probe beam monitors the change [24, 25]. However, the technique requires an embedding environment with a high photothermal response, which is impractical. In addition, a nano-object can cause a spectral shift in the resonance wavelength of a nanophotonic structure, providing a signature of the nano-object. Examples of such structures include a nanorod [26], nanowires [27], photonic crystals [28], ring resonators [29], and photonic waveguides [30]. However, the sensitivity is extremely low, using nanophotonic structures; for example, there is a < 0.01 nm wavelength change for a 1 nm change in diameter of nano-object [31, 32]. The low sensitivity also inhibits the detection of sub-15 nm objects.

In this work, we introduce a completely different approach to boost the detection sensitivity and the scattered intensity of nano-objects. We consider the nano-object as a resonator that can strongly couple to a plasmonic nanocavity. The coupling between the elastic scattered intensity of the two systems needs to exceed both the cavity loss rate and the scattering loss rate of the nano-object for energy exchange between the nano-object and nanocavity [33]. If the strong coupling condition is fulfilled, we expect

that two scattering modes will appear and their spectral shift will be highly dependent on the properties of the nano-object. However, this approach has been unexplored so far.

Strong coupling has been widely observed in several systems where light and matter are hybridized and new dressed states arise. Typically, this condition involves an optical cavity and either an electronic (vibronic) state (e.g. in an atom [34, 35], quantum dot [36–38], two-dimensional material [39, 40], or single molecule [41–44]) or a molecular vibrational state [45–47]. On the other hand, there is no demonstration of elastic scattering strong coupling to detect small nano-objects, even though elastic scattering is universal to all objects due to refractive index contrast.

This paper presents an experimental and numerical demonstration of elastic scattering strong coupling to detect single sub-15 nm nano-object. The nano-object strongly couples with a plasmonic nanocavity, which is formed by a Au nanoparticle placed on top a Au film. The strongly coupled system reveals two modes in darkfield extinction spectroscopy that strongly depend on the cavity and nano-object parameters. We demonstrate that this effect applies to metallic nano-objects such as gold, silver, aluminum, and copper. Employing elastic light scattering strong coupling, establishes a new possibility of observing small, non-fluorescent, Raman inactive objects.

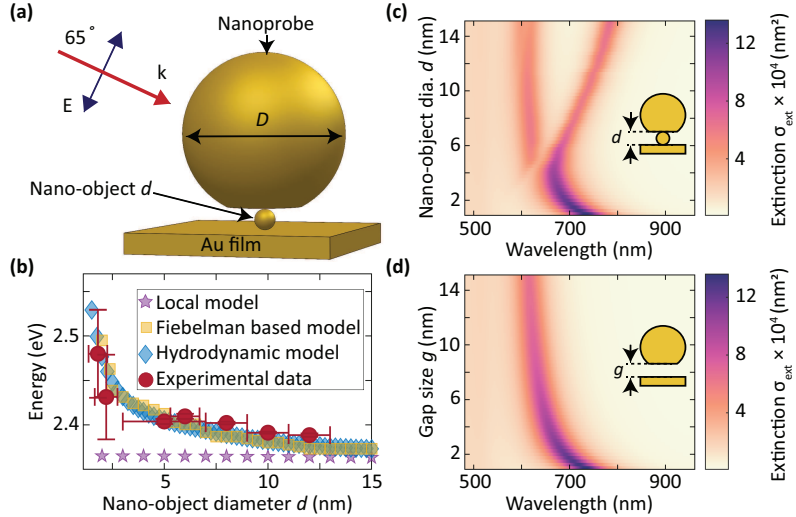


Fig. 1 (a) Schematic of the sample that consists of a faceted Au nanoparticle (nanoprobe) with diameter D and a nano-object with diameter d that is placed on top of the Au film. The incident angle of light is 65° . (b) Plasmon resonance of sub-15 nm Au nano-objects in water, outside the nanocavity. (c) Extinction cross-section (σ_{ext}) spectra of a Au nano-object inside nanocavity for different nano-object diameters. (d) Extinction cross-section (σ_{ext}) spectra of an empty nanocavity with different gap size g . In (c) and (d), the Au nanoprobe diameter $D = 80$ nm and $g = d$.

2 Modes of a Au nano-object inside a plasmonic nanocavity

We first perform numerical calculations to understand the interactions of a single nano-object and a plasmonic cavity by solving the full Maxwell equations using the boundary element method [48–50] and finite element method (for numerical setup, see Methods). A broadband light source with transverse magnetic polarization illuminates the structure at an angle of 65° (Fig. 1a, see Supplementary Information, SI.A). The diameter d of the nano-object varies from 1 nm to 15 nm, and the diameter of the nanoprobe is 80 nm. We account for non-local effects that are dominant at smaller sizes (< 20 nm) of the nano-objects [51]. In hydrodynamic model, a composite object consisting of the nano-object and a thin layer coating with effective permittivity models the non-local effects. In a model based on Feibelman parameters, a mesoscopic boundary condition is applied to include the non-local effects (see Methods).

Our starting point is the plasmon resonance of the nano-object outside the nanocavity environment. The non-local hydrodynamic model shows a pronounced resonance shift of up to 180 meV as the diameter of the nano-object decreases from 15 nm to 1 nm (Fig. 1b). The result of using the Feibelman parameters agrees well with the non-local hydrodynamic model. In contrast, a local (Drude) model shows no pronounced spectral shift. To verify these numerical results, we experimentally probe the plasmon resonance of Au nano-objects in a colloidal solution and observe that the plasmon resonance from the non-local model and Feibelman-based model agrees with the experimental results. These results align with the well-established understanding that as the nanoparticle diameter decreases below 20 nm, the plasmon resonance shifts towards higher energies [52]. The spectral shift is due to spatial dispersion of the dielectric function $\varepsilon(\mathbf{r}, \mathbf{r}')$, and this means that the dielectric function contributes to the displacement field at positions \mathbf{r} , which is non-local to the position \mathbf{r}' of the excitation electric field [53–55].

We calculate the scattering spectrum of the nano-object inside the nanocavity using the hydrodynamic model due to its accuracy and fast computation speed to investigate a wide range of sample parameters space. There is a remarkable difference between the extinction spectra when a nano-object is in the gap compared to an empty nanocavity (Figs. 1c,d). Two plasmonic modes appear for nano-objects with diameters $d > 4$ nm, and only one mode is visible for $d < 4$ nm. The longer wavelength mode strongly depends on d , while the lower wavelength mode closely follows the mode of the empty nanocavity. We establish the origin of these modes in the following section below. These modes show a nonlinear wavelength dependence on the diameter of the nano-object, thus resulting in a high sensitivity. There is a maximum wavelength change of 70 nm for a 1 nm change of d (see SI.B for more details). For the empty nanocavity, a dipolar mode due to the coupling between the nanoprobe and the image charge persists for all gap spacing [56, 57]. This mode is also present in the scattering and absorption cross-section spectra (see SI.C) and we refer to the mode as the nanocavity mode.

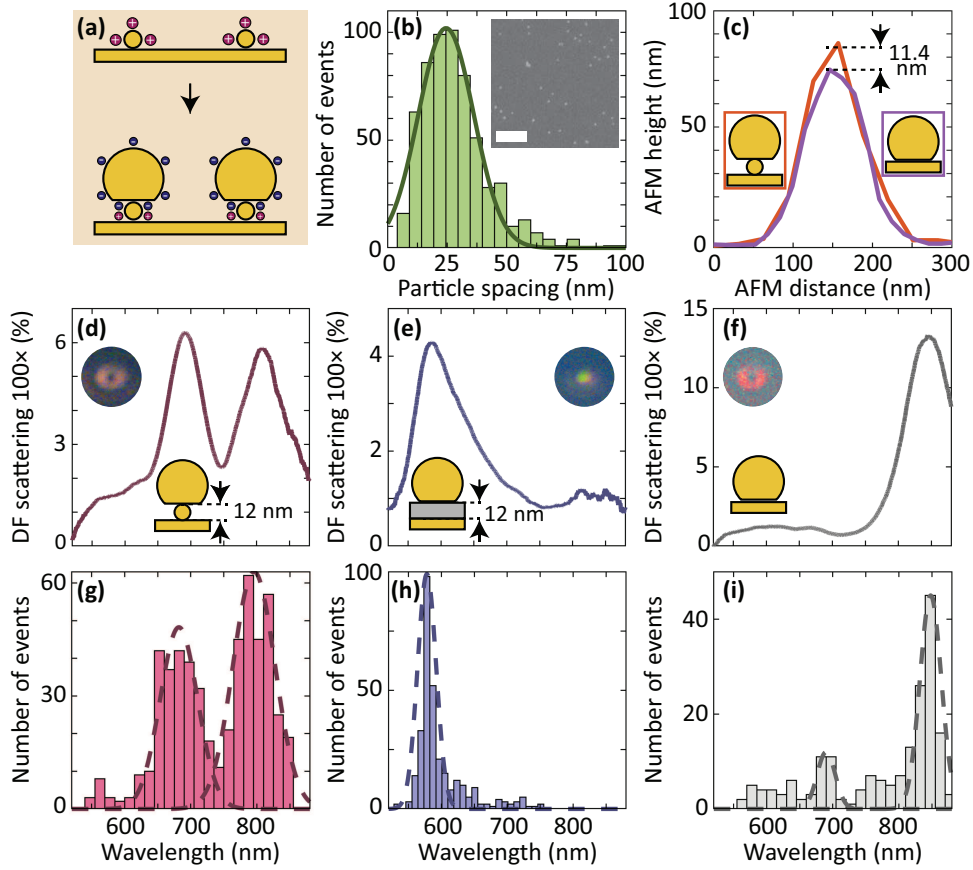


Fig. 2 (a) Schematic of the sample fabrication process, which includes depositing the positively charged nano-object on the Au film (top) and forming the nanocavity due to electrostatic attraction of the nano-object and negatively charged nanoprobe (bottom). (b) The spacing distribution between the nano-objects determined from the scanning electron microscope in the inset. The scale bar of the inset is 200 nm. (c) The AFM height measurement of an empty nanocavity (purple line) and a nanocavity with a 12 nm nano-object inside the gap (orange line). (d-f) The dark-field spectra of a nanocavity with (d) a 12 nm nano-object inside the gap, (e) a dielectric layer filled the gap, (f) nanoparticle directly on the Au film. In (d)-(f), the insets show the dark-field image of the corresponding nanocavity. (g-i) The histogram of the scattering peak measured nanocavities for (g) a 12 nm nano-object inside the gap, (h) a dielectric layer filled the gap, (i) an empty gap. The dashed line is a Gaussian fit to the detected maxima in the histogram. In (a)-(i), the nanoprobe diameter is 80 nm.

3 Experimental probe of a single nano-object in the nanocavity

To experimentally confirm the modes described above, we fabricate plasmonic nanocavities with a nano-object inside the gap. The nanoprobe assembles directly on the nano-object on a Au film using electrostatic attraction (Methods). The surfaces

of the nanoprobe and nano-object are oppositely charged due to the capping agents of citrate and cysteamine hydrochloride, respectively (Fig. 2a).

We first deposited several 12 nm nano-objects on Au film (inset, Fig. 2b). The surface density of the nano-objects is aimed to be 1600 particles/ μm^2 , to obtain an average particle spacing of 25 nm. This surface density ensures that on average only one nano-object is under the probe facet [58]. Based on the SEM image analysis, the nano-object spacing with the highest occurrence frequency is 24.5 nm, as expected (Fig. 2b). To confirm that the nano-objects are inside the nanocavity, we use an atomic force microscope (AFM) to measure the height of the nanocavities on two different samples: (1) the probe on top of the nano-object (12 nm in diameter) on the Au film and (2) the probe directly on the Au film. There is an 11.4 ± 3.3 nm height difference between the maximum height of a nanocavity with the 12-nm object inside the gap and an empty nanocavity (Fig. 2c, see SI.D for more statistics). This result shows that the nano-object assembles under the probe.

We use a custom-made dark-field micro-spectrometer to acquire scattering images and the extinction spectrum to probe the resonance of the compound structure (see SI.E for experimental setup). For a single nano-object ($d = 12$ nm) inside the nanocavity, there are two dominant resonant modes at 690 nm and 807 nm (Fig. 2d). This experimental observation is consistent with the simulation results that also reveal two modes. To further prove that these modes are due to the Au nano-object in the gap, we compare the modes to that of two other samples: (1) a nanocavity with a dielectric layer (aluminum oxide) with thickness 12 nm, which is equal to d and (2) an empty nanocavity that has the Au probe directly on the Au film. The nano-object-in-nanocavity modes are significantly different from the modes of these two samples (Figs. 2e,f). There is a single plasmonic mode in the dark-field spectrum of nanocavity with a dielectric-filled gap and empty gap at 585 nm and 844 nm, respectively. These modes are the dominant nanocavity modes with different gap sizes. The dielectric-filled nanocavity has a blue-shifted resonance compared to the empty nanocavity because of the larger gap size.

Far-field scattered intensity profiles provide additional information about the nature of the modes of the nano-object-in-the-cavity structure [59]. The nano-objects alone are not visible in the dark-field image due to the low scattering cross-section. On the other hand, the nano-object-nanocavity compound structure scatters light significantly, such that there is a high contrast between the structure and the Au film (insets, Figs. 2d-f). The scattering image from the nano-object inside the nanocavity and the empty nanocavity is a ring-shaped donut pattern. This far-field scattering pattern is due to the electric field that is z -polarized inside the nanocavity, and the z -orientated dipole dominates the far-field emission [60, 61]. However, the dielectric-filled gap nanocavity shows a spot pattern due to the transverse plasmonic mode of the nanoparticle.

We further measured the dark-field scattering spectrum from more than 700 nanocavities with a nano-object inside the gap, dielectric-filled gap, and empty gap (Figs. 2g-i). For each structure, the peak wavelength of the resonance modes was determined using a Gaussian distribution fit to the histogram maxima. There are two dominant peaks at 682 nm and 796 nm for 12 nm nano-objects inside the nanocavity,

while the dielectric-filled gap nanocavity and empty nanocavity have a single dominant peak at 578 nm and 848 nm, respectively. The histograms provide sufficient statistics to demonstrate the consistency of the modes.

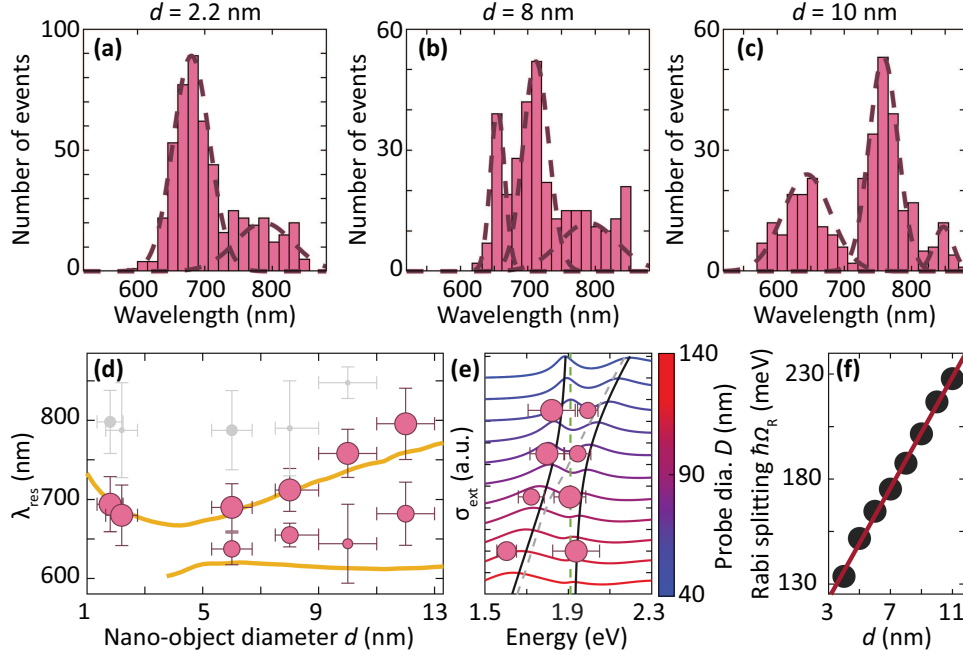


Fig. 3 The histogram of the scattering peak of the measured nanocavities with a (a) 2.2 nm, (b) 8 nm, and (c) 10 nm nano-object inside the nanocavity. The dashed line is a Gaussian fit to the histogram. (d) The resonance wavelength of Au nano-object with a diameter of 1.8 nm to 12 nm inside a nanocavity measured experimentally (pink circles) and simulation result from Fig. 1c (yellow line). The size of the markers are determined by the relative occurrence frequency in each histogram. The vertical error bar is determined from the standard deviation of the Gaussian distribution fit to the histograms, and the horizontal error bar is determined by the size variation of the nano-objects obtained from the manufacturer. The gray markers are the scattering peaks that have a much lower occurrence frequency, and they are attributed to the presence of more than one nano-object inside the gap. (e) Experimentally measured resonance energy of an Au nano-object with a diameter of 6 nm inside a nanocavity for different nanoprobe diameters (pink circle). The blue-to-red colored lines are the simulated extinction cross-section spectra of a 6 nm nano-object inside a plasmonic nanocavity. The black lines are based on a strongly coupled resonator model. The resonance of the nano-object on the Au film is the green dashed line, and that of the nanoprobe on the film is the gray dashed line. (f) Extracted Rabi splitting (Ω_R) vs the nano-object diameter. The line shows a linear fit from an analytical mode.

4 Size dependence of the nano-object-in-cavity mode

We investigate the dependence of the nano-object-in-cavity modes on the nano-object diameter from 1.8 nm to 12 nm and interrogated > 250 structures for each diameter. The resonance modes of 8 nm and 10 nm nano-objects in the nanocavity show two

strong peaks at (655, 712) nm and (644, 758) nm, respectively, while the 2.2 nm nano-objects show one strong peak at 680 nm (Figs. 3 a-c). A peak with a lower occurrence frequency appears at around 800 nm for 2.2 nm and 8 nm nano-objects. We attribute this peak to nanocavities that have more than one nano-object (see Fig. F6). There is a broader distribution of the resonance peaks for nanocavities with a nano-object compared to empty and dielectric-filled nanocavities. We attribute this broadening to the large variation in d of the nano-objects, as supplied by the manufacturer (SI).

We further extract the peak wavelength of all the scattering modes from the histograms for different nano-object diameters. There are two resonance modes for nano-objects from 12 nm down to 6 nm, while the smaller nano-objects show one dominant mode (Fig. 3d). The higher wavelength mode shows a stronger dependence on d than the lower wavelength mode. The measured resonances agree well with the simulation results (yellow line) extracted from Fig. 1c. The lower wavelength mode slightly deviates (~ 15 nm) from the simulation results, which might be due to experimental parameters (e.g., the polyhedral shape of the probe, specific vertical arrangement of the probe, etc) that are not accounted for in the simulations. Overall, the experimentally observed modes are reproduced in the simulation. The data marker size is determined by the relative occurrence frequency of the mode in each histogram. The vertical error bar is determined from the standard deviation of the Gaussian distribution fit to the histograms, and the horizontal error bar is from the distribution of the nano-object size obtained from the manufacturer.

5 Strong coupling of nano-object and plasmonic nanocavity

To understand the origin of the nano-object-in-cavity mode, we describe the interaction of the nano-object in the plasmonic nanocavity using a simple model of two coupled oscillators. The oscillators are the nano-object on the Au film and the nanocavity with the probe close to the Au film. We simulate the extinction of these two systems separately and tune the resonance of the nanocavity by changing the probe size. The energy E^\pm of the resonance of two strongly coupled systems can be described using [62]

$$E^\pm = \frac{E_{\text{nc}} + E_{\text{no}}}{2} \pm \frac{1}{2} \left[(\hbar\Omega_{\text{R}})^2 + (E_{\text{nc}} - E_{\text{no}})^2 \right]^{1/2}, \quad (1)$$

where E_{nc} and E_{no} are the energy of the nanocavity mode and the nano-object on Au film, respectively. The E_{no} also includes perturbation of the resonance of the nano-object due to an increased electron density in the gap (for further simulations and analysis, see SI). We obtain Rabi splitting $\hbar\Omega_{\text{R}}$ as the energy separation between the uncoupled modes at the avoided crossing where the two resonance energies.

For a 6 nm nano-object in the nanocavity, the two modes consistently occur at different nanocavity resonances (Fig. 3e). The energies of the modes follow a clear anti-crossing behavior, which fits well with the theoretical model (Eq. 1). The extinction spectrum becomes broader at larger nanoprobe diameters due to increased damping by the larger nanoparticles [53]. Experimentally, we tune the nanocavity resonance using probe diameters between 60 - 125 nm. The experimental result also follows the

strong coupling model in agreement with the simulation results. The Rabi splitting ($\hbar\Omega_R = 0.165$ eV) overcomes both the nano-cavity loss ($\gamma_{nc} = 0.09$ eV) and nano-object on Au mirror loss ($\gamma_{no} = 0.04$ eV), indicating that the hybrid nano-object inside the nanocavity system is above the onset of the strong coupling regime (see SI.H for further analysis). We extract the Rabi splitting of different nano-object diameters from the numerical calculations. The Rabi splitting linearly increases from 130 meV to 230 meV for nano-object diameters 4 nm to 11 nm (Fig. 3f). The linear trend agrees with a simple model that we obtain for the Rabi splitting $\Omega_R = \frac{8}{3}\mu_m \frac{d}{D} \sqrt{\frac{2\pi c N_n}{3\hbar\lambda\epsilon r_0}}$, where μ_m is the transition dipole moment of nano-object, \hbar is Planck constant, c is the light speed, N_n is the metal atom density, r_0 is the atom radius and ϵ is the permittivity of the medium inside the nanocavity gap, which includes the permittivity of the nano-object and air.

We extend our investigation to include nano-objects that are made of different metallic materials, to understand the effect of different dielectric functions of the nano-objects. We calculate the extinction cross-section of single gold, silver, aluminum, and copper nano-objects inside the plasmonic nanocavity (see SI.J). We tune the resonance of the nanocavity for copper and silver nano-objects with a diameter of 6 nm (Fig. 4a). Two modes also appear in the extinction spectra for both nano-objects with different nanoprobe diameters, which follow the strong coupling model. As the diameter of the nanoprobe increases, the relative peak value of the higher-energy mode decreases in comparison to that of the lower-energy mode. This is as a result of the larger nanoprobe size than the nano-object, which contributes more to the total extinction spectrum. We extract the Rabi splitting for gold, silver, aluminum, and copper nano-objects. There is a linear increase of the coupling strength to the plasma frequency (ω_p) of the nano-object (Fig. 4c). This linear trend agrees well with an analytical model that describes the coupling strength as $\Omega_R = \omega_p \frac{\mu_m}{e} \sqrt{\frac{cmV_n}{\hbar\lambda\epsilon V_m}}$ (see SI.K), where e is electron charge, m is the effective electron mass, V_m is the nanocavity mode volume and, V_n is the nano-object volume.

6 Scattering cross-section ratio

We now investigate how the nanocavity modifies the scattering cross-section of the nano-object, such that its signature is now observable in our measurements. In the weak coupling regime, far from the anti-crossing point, the longer wavelength mode tends to the resonance wavelength of the nano-object inside the cavity. Therefore, we compare the scattering cross-section of this longer wavelength mode to the resonance wavelength of the nano-object outside the nanocavity environment. We define η_{sca} as the ratio of the scattering cross-section of the longer wavelength mode (σ_{sca}^i) to the scattering cross-section of nano-object mode outside of the nanocavity (σ_{sca}^o) *i.e.*, $\eta_{sca} = \frac{\sigma_{sca}^i}{\sigma_{sca}^o}$, with the superscripts i and o indicating the σ_{sca} inside and outside the cavity, respectively. We consider the σ_{sca} at about 100 nm (0.3 eV) away from the anti-crossing point. The scattering ratio represents the efficiency of the nanocavity to boost the scattering cross-section of the nano-object, which is otherwise extremely challenging to detect in air.

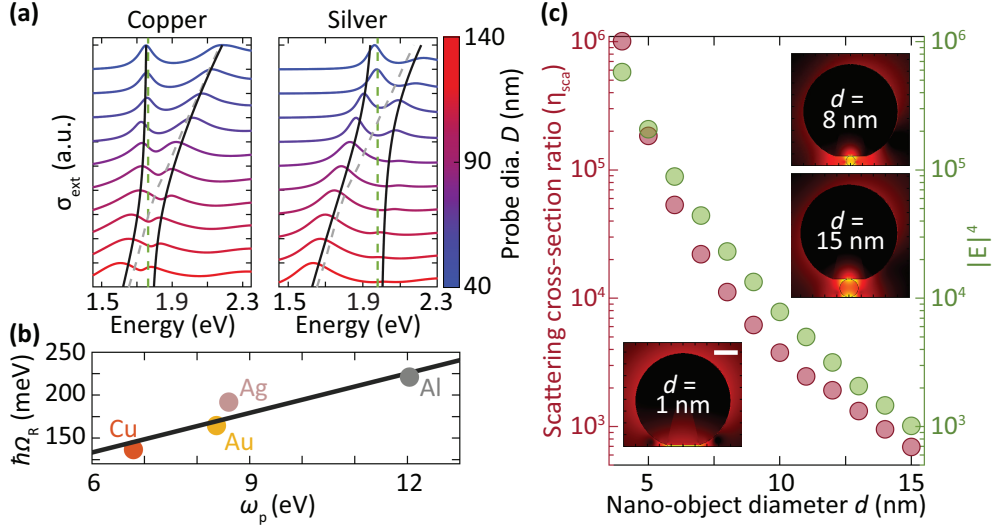


Fig. 4 (a) Normalized extinction cross-section (σ_{ext}) spectra of a copper nano-object (left) and a silver nano-object (right) inside nanocavity with different nanoprobe diameters. The black lines are based on the strongly coupled resonator model. The resonance of the nano-object on the Au film is the green dashed line, and that of the nanoprobe on the film is the gray dashed line. The diameter of the nano-object is 6 nm. (b) Rabi splitting of different nano-objects *vs* plasma frequency ω_p . The line shows a linear fit from the analytical model. (c) Calculated scattering cross-section ratio of Au nano-object inside a nanocavity (red circle). The averaged electric field over the area of the nano-object $|E|^4$ in the gap of an empty nanocavity (green circle). The inset shows the electric field distribution of a nano-object in nanocavity. The nanoprobe diameter is 80 nm, and the scale bar is 20 nm.

There is a η_{sca} of 10^6 for 4 nm nano-object, and it decreases to 10^3 as the diameter of the nano-object increases to 15 nm (Fig. 4c). This implies that the nano-object exhibits a much larger scattering cross-section, thanks to the nanocavity. To understand the origin of the scattering ratio, we calculate the electric field enhancement distribution inside a nanocavity without the nano-object and average the electric field over the area of the nano-object inside the gap. The trend of the electric field $|E|^4$ *vs* d is similar to that of the scattering cross-section ratio (Fig. 4c). There is a deviation of less than one order of magnitude for larger nano-objects, and we attribute this deviation to the increased detuning of the nanocavity mode and nano-object on Au film, which decreases the scattering cross-section ratio. The nanocavity localizes the electric field on the nano-object inside the gap (insets, Fig. 4c), resulting in the up to 10^6 scattering cross-section ratio of the nano-object.

7 Discussion and conclusion

We have achieved elastic light scattering strong coupling between a sub-15 nm nano-object and a plasmonic nanocavity. Experimental and numerical results show a clear modification of the extinction spectra due to the presence of the nano-object in the cavity, revealing the signatures of nano-objects down to 1.8 nm. In addition, the extinction spectra reveal a clear anti-crossing behavior for nano-objects between 4 nm

and 15 nm. Our results further show that the coupling strength is dependent on the plasma frequency of the nano-object in addition to their size. In comparison to free space, the nanocavity boosts the scattering cross-section by up to 10^6 , which enables the observation of the nano-object. Moreover, this scattering cross-section ratio scales with the electric field to the fourth power inside the plasmonic nanocavity, similar to surface-enhanced Raman spectroscopy.

Our work establishes a new possibility for exploring the strong coupling of elastic scatterers with cavities under ambient conditions. This is the first demonstration of strong coupling of elastic scattering of non-fluorescent, Raman inactive sub-15 nm objects. Our approach holds promise for accurate imaging and detecting small nano-objects in a low-cost and easy-to-use manner. The strong coupling effect provides a nonlinear wavelength dependence on the nano-object diameter, which results in a high sensitivity. Given the universal nature of elastic scattering, we anticipate applications in nanosensing and nanotechnology characterization of metallic nano-objects. We foresee that future work will demonstrate the applicability to dielectric materials, which are in the weak coupling regime. The technique introduced here can complement electron microscopes and scanning probes for optical characterization. A nanoprobe attached to a cantilever can scan above the nano-object, which does not require surface modification.

8 Methods

8.1 Numerical setup

We solve the full Maxwell's equation using the boundary element method (BEM). The BEM is suitable for metallic nanostructures with abrupt interfaces that are embedded inside a homogeneous and isotropic dielectric medium. In addition, arbitrary shapes and sizes can be defined and computed with reasonable computational resources [49]. The approach is suitable for simulating metallic nanoparticles with sizes ranging from a few to a few hundreds of nanometers [49, 50]. The main advantage of the BEM approach over others (e.g. finite element method and finite difference time domain) is the speed of the computations, which enables us to explore a wide range of parameters.

We obtain the scattering cross-section and the extinction cross-section in the far-field and electric field distribution in the vicinity of the nanostructures. In the simulations presented in this paper, the dielectric function of gold is taken from the Johnson and Christy database [63] for nanocavity and the non-local model for nano-object. We use a perfectly spherical particle, described by the "trisphere" function in the MNPBEM MATLAB toolbox [49]. This function loads points on a sphere from a file and performs triangulation. It is known that the metallic nanoparticles are inevitably faceted. As a simplistic model that is relevant for experimental purposes, we simulate a faceted particle with a facet ratio $w/D = 0.375$, where w and D are facet size and the diameter of the nanoprobe. We choose this facet ratio based on previous measurements [58, 64]. To realize the faceted-sphere structure, we cut the bottom side of a perfect sphere at $Z_{cut} = \sqrt{((D/2)^2 - w^2)}$ and then combine it with a 2D surface using the "polygon" function.

The structure shown in Fig. 1a is excited by a plane wave. The incident angle of the plane wave is 65 degrees due to the illumination angle in the dark-field scattering experiment. The polarization of the incident light is transverse magnetic with an amplitude of E_0 which is the unit amplitude in calculating electric field enhancement. The Au particle and the object are surrounded by air ($n = 1$) on top. The simulated wavelength range covered 482.5–960 nm, with a spacing of 2.5 nm (192 spectral points). We used a supercomputer (Snellius, Dutch National computer) with 48 nodes (Genoa), each node consisting of 192 cores and 1440 GB RAM capacity. Depending on the nanoprobe diameter and nano-object diameter, the computation time ranges from 9 minutes to 150 minutes per spectrum.

8.2 Non-local hydrodynamic model

Surface plasmons on metal surfaces can concentrate light into sub-nanometric volumes. However, at scales near the Thomas-Fermi screening length, the electric response at the metal interface must be considered smeared out rather than localized. This understanding is crucial for modeling small metallic nano-objects. We start with the polarizability of a spherical nano-object, including non-local effects, that is described by [65]:

$$\alpha_{\text{p}}^{\text{NL}} = 4\pi R^3 \left\{ \frac{\frac{\varepsilon_{\text{m}}}{\varepsilon_{\text{b}}} - \left[1 + \frac{\varepsilon_{\text{m}} - \varepsilon_{\text{b}}}{\varepsilon_{\text{b}} q_{\text{L}} R} \frac{i_1(q_{\text{L}} R)}{i_1'(q_{\text{L}} R)} \right]}{\frac{\varepsilon_{\text{m}}}{\varepsilon_{\text{b}}} + 2 \left[1 + \frac{\varepsilon_{\text{m}} - \varepsilon_{\text{b}}}{\varepsilon_{\text{b}} q_{\text{L}} R} \frac{i_1(q_{\text{L}} R)}{i_1'(q_{\text{L}} R)} \right]} \right\}. \quad (2)$$

Here $q_{\text{L}} = \sqrt{\omega_{\text{p}}^2 / \varepsilon_{\infty} - \omega(\omega + i\Gamma)} / \beta$ represent the longitudinal plasmon wavevector and i_1 is the modified spherical Bessel function of the first kind and its derivative, β is proportional to the Fermi velocity, ε_{b} is the dielectric function of the surrounding environment, and R is the radius of the nano-object. The metal is characterized by a spatially dispersive permittivity tensor given by: $\varepsilon_{\text{m}}(\omega) = \varepsilon_{\infty} - \omega_{\text{p}}^2 / [\omega(\omega + i\Gamma)]$, where ε_{∞} is the dielectric background, Γ and ω_{p} denote the metal damping and plasma frequency.

One can accurately reproduce the effects of non-locality using a model that replaces a non-local metallic surface with an effective local metallic surface coated with a dielectric layer. The polarizability of a metallic nano-object with a thin dielectric layer of Δd can be obtained from [54]:

$$\alpha_{\text{p}}^{\text{L}} = 4\pi R^3 \left\{ \frac{\frac{\varepsilon_{\text{m}}}{\varepsilon_{\text{b}}} - \frac{R}{R - \Delta d} \left(1 + \frac{\varepsilon_{\text{m}}}{\varepsilon_{\text{t}}} \frac{\Delta d}{R} \right)}{\frac{\varepsilon_{\text{m}}}{\varepsilon_{\text{b}}} + \frac{2R}{R - \Delta d} \left(1 + \frac{\varepsilon_{\text{m}}}{\varepsilon_{\text{t}}} \frac{\Delta d}{R} \right)} \right\}. \quad (3)$$

Comparing equations 3 and 2 and assuming that the dielectric layer is isotropic, the permittivity of the dielectric coating layer is given by [54]:

$$\varepsilon_{\text{t}} = \left(\frac{\varepsilon_{\text{b}} \varepsilon_{\text{m}} q_{\text{L}} \Delta d}{\varepsilon_{\text{m}} - \varepsilon_{\text{b}}} \right) \frac{i_1'(q_{\text{L}} R)}{i_1(q_{\text{L}} R)}. \quad (4)$$

Using a dielectric coating layer around the metallic nano-object with a diameter of 1 nm to 15 nm with the dielectric function introduced in the equation 4 was used to account for non-locality effects.

8.3 Mesoscopic electromagnetic boundary condition

Utilizing mesoscopic boundary conditions is another approach that accounts for quantum mechanical mechanisms such as non-locality. It can correct the electromagnetic response and adjust the local classical simulation results that may deviate from experimental observations. We use a general theoretical framework based on Feibelman d -parameters to model the electromagnetic response of sub-15 nm nano-objects [66]. Yang et al. amend the classical electromagnetic boundary condition (Eq. 5) through mesoscopic surface-response formalism by the Feibelman d_{\perp} and d_{\parallel} parameters (Eq. 6).

$$\begin{aligned} D_{\perp}^{+} - D_{\perp}^{-} &= 0 \\ B_{\perp}^{+} - B_{\perp}^{-} &= 0 \\ \mathbf{E}_{\parallel}^{+} - \mathbf{E}_{\parallel}^{-} &= \mathbf{0} \\ \mathbf{H}_{\parallel}^{+} - \mathbf{H}_{\parallel}^{-} &= \mathbf{0} \end{aligned} \quad (5)$$

$$\begin{aligned} D_{\perp}^{+} - D_{\perp}^{-} &= d_{\parallel} \nabla_{\parallel} \cdot (\mathbf{D}_{\parallel}^{+} - \mathbf{D}_{\parallel}^{-}) \\ B_{\perp}^{+} - B_{\perp}^{-} &= 0 \\ \mathbf{E}_{\parallel}^{+} - \mathbf{E}_{\parallel}^{-} &= -d_{\perp} \nabla_{\parallel} (E_{\perp}^{+} - E_{\perp}^{-}) \\ \mathbf{H}_{\parallel}^{+} - \mathbf{H}_{\parallel}^{-} &= i\omega d_{\parallel} (\mathbf{D}_{\parallel}^{+} - \mathbf{D}_{\parallel}^{-}) \times \hat{\mathbf{n}}, \end{aligned} \quad (6)$$

which $d_{\perp}(\omega) = \frac{\int dx x \rho(x, \omega)}{\int dx \rho(x, \omega)}$ and $d_{\parallel}(\omega) = \frac{\int dx x \partial_x J_y(x, \omega)}{\int dx \partial_x J_y(x, \omega)}$, represent the frequency-dependent centroids of the induced charge $\rho(x, \omega)$ and the normal derivative of the tangential current $J_y(x, \omega)$. The first Feibelman parameter, $d_{\perp}(\omega)$ is sufficient to describe most problems invoking metal surfaces and $d_{\parallel}(\omega) = 0$ on a metal-dielectric interface.

We use COMSOL Multiphysics to implement the mesoscopic boundary condition via the auxiliary potential method for sub-15 nm nano-objects. To improve the numerical stability, an integral form of weak constraints is used. The results of the simulations using mesoscopic boundary conditions agree with the experimental results and nonlocal hydrodynamic model. However, the computational time using mesoscopic boundary conditions increased by about an order of magnitude in 2D while the nonlocal hydrodynamic simulations were performed in 3D.

8.4 Sample fabrication

Materials: The Au nano-objects with diameters of 6 nm, 8 nm, 10 nm, and 12 nm were purchased from Aurion. The 1.8 nm, 2.2 nm, and 125 nm nanoparticles were obtained from Nanopartz. The 60 nm, 80 nm, and 100 nm nanoparticles, and cysteamine hydrochloride were purchased from the BBI solutions.

Template-stripping: We use the template-stripping technique to obtain the Au substrate. A silicon wafer was coated with a 100 nm layer of Au by thermal vapor deposition with a deposition rate of 0.3 Å/s. Then, the surface of the Au was coated with a thin layer of UV epoxy (Thorlabs, NOA81), and 8 mm round glasses were glued to the surface. The substrate was exposed to a UV light for 20 minutes. The glass substrates glued to the Au film on the initial wafer can be stored at room temperature in the air and peeled off as required.

Au nanoparticle functionalizing: It is possible to use a similar surface modification technique for metals in general. Here, we choose gold nanoparticles for their inherent stability, resistance to oxidation under ambient conditions, and wide commercial availability in various sizes. In this work, we use 11 different Au nanoparticles with diameters from 1.8 nm to 125 nm.

The nanoprobe is functionalized with citrate, which is negatively charged due to the carboxylate group. The Au nano-objects are reactant-free and ready for functionalization. We use cysteamine to functionalize the surface of nano-objects. Cysteamine has a thiol group and an amino group where it can form a bond with the Au surface through the thiol group. The amino terminal group is positively charged, which attracts the negatively charged nanoprobe through electrostatic attraction.

Concentration of cysteamine: Controlling the concentration of the cysteamine is crucial because excessive cysteamine on the surface of the Au nano-object results in a change in the resonance of the nano-object and can possibly cause aggregation of the nano-objects. We vary the cysteamine concentration from 1 μM to 20 μM , and the results indicate that 1 μM is the optimal concentration due to the minimal change in the optical properties of the nano-object (Fig. L12). We use the absorbance ratio at 680 nm and 518 nm to determine the changes in the plasmon resonance of the nano-object. We use a 1:1 volume ratio of cysteamine solution and colloidal Au nano-objects.

Au nanoparticle assembly: To deposit the cysteamine-coated nano-object on the Au substrate, we dried the solution of the nano-objects on the Au substrate. We choose the concentration of the nano-object based on the nanoprobe facet size to avoid having more than 1 nano-object in the nanocavity but also provide sufficient nano-object on the surface. To assemble the nanoprobe on the nano-object, we drop cast the solution of the nanoprobe on the Au substrate with already fixed nano-objects. The deposition time of the nanoprobe determined the number of the formed nanocavities. We tuned the deposition time to ensure only one nanocavity is measured per time, and eventually, a 120-second deposition time was chosen. Finally, we rinsed the sample with deionized water to remove the unbonded nanoprobe.

Dielectric layer-filled gap and empty gap nanocavities: To obtain nanocavity with an empty gap, we dropcast the probe on the template-striped Au film for 5 minutes. We also fabricate nanocavities with a dielectric layer-filled gap by coating a 12 nm aluminum oxide (Al_2O_3) layer using electron-beam deposition. We use quartz crystal microbalance to measure the thickness of the coated layer, and a final thickness of 11.40 nm is obtained. Subsequently, nanoprobe is drop-casted on the Al_2O_3 coated Au film to form dielectric layer-filled gap nanocavities.

Acknowledgements. We acknowledge the Faculty of Science and Technology, the University of Twente, for a tenure-track start-up package. This publication is part of the project "Observing objects that evade light" with project number OCENW.XS23.1.198, which is financed by the Dutch Research Council. This work used the Dutch national e-infrastructure with the support of the SURF Cooperative using grant no. EINF-8959. We are thankful to Robert Molenaar and Melissa Goodwin for technical help in characterizing the samples, and Mike Dikkers for gold and aluminum oxide coating. We are also grateful to Ulrich Hohenester for the useful discussion, Herman Offerhaus for feedback, and Mireille Claessens for lab space and equipment.

References

- [1] Kulkarni, K. S. *Nanotechnology: principles and practices* (Springer, USA, 2015).
- [2] Dimitratos, N. *et al.* Strategies to improve hydrogen activation on gold catalysts. *Nature Reviews Chemistry* 1–16 (2024).
- [3] Zijlstra, P. & Orrit, M. Single metal nanoparticles: optical detection, spectroscopy and applications. *Reports on Progress in Physics* **74**, 106401 (2011).
- [4] Wang, X., Huang, S.-C., Hu, S., Yan, S. & Ren, B. Fundamental understanding and applications of plasmon-enhanced raman spectroscopy. *Nature Reviews Physics* **2**, 253–271 (2020).
- [5] Ma, X. *et al.* Single gold-bridged nanoprobe for identification of single point dna mutations. *Nature communications* **10**, 836 (2019).
- [6] Xu, M. *et al.* Size-dependent in vivo transport of nanoparticles: implications for delivery, targeting, and clearance. *ACS nano* **17**, 20825–20849 (2023).
- [7] Li, L. *et al.* Current strategies of photoacoustic imaging assisted cancer theragnostics toward clinical studies. *ACS Photonics* **9**, 2555–2578 (2022).
- [8] Dolai, J., Mandal, K. & Jana, N. R. Nanoparticle size effects in biomedical applications. *ACS Applied Nano Materials* **4**, 6471–6496 (2021).
- [9] Zhao, X. *et al.* Transistors and logic circuits based on metal nanoparticles and ionic gradients. *Nature Electronics* **4**, 109–115 (2021).
- [10] Zhang, F., Wang, Z., Peijnenburg, W. J. & Vijver, M. G. Review and prospects on the ecotoxicity of mixtures of nanoparticles and hybrid nanomaterials. *Environmental Science & Technology* **56**, 15238–15250 (2022).
- [11] Zhou, R., Edwards, C., Arbabi, A., Popescu, G. & Goddard, L. L. Detecting 20 nm wide defects in large area nanopatterns using optical interferometric microscopy. *Nano letters* **13**, 3716–3721 (2013).

- [12] Sani, A., Cao, C. & Cui, D. Toxicity of gold nanoparticles (aunps): A review. *Biochemistry and biophysics reports* **26**, 100991 (2021).
- [13] Bohren, C. F. & Huffman, D. R. *Absorption and Scattering of Light by Small Particles* (John Wiley & Sons, New Jersey, USA, 1998).
- [14] Crut, A., Maioli, P., Del Fatti, N. & Vallée, F. Optical absorption and scattering spectroscopies of single nano-objects. *Chemical Society Reviews* **43**, 3921–3956 (2014).
- [15] Zhou, J., Chizhik, A. I., Chu, S. & Jin, D. Single-particle spectroscopy for functional nanomaterials. *Nature* **579**, 41–50 (2020).
- [16] Hell, S. W. & Wichmann, J. Breaking the diffraction resolution limit by stimulated emission: stimulated-emission-depletion fluorescence microscopy. *Optics letters* **19**, 780–782 (1994).
- [17] Orrit, M. & Bernard, J. Single pentacene molecules detected by fluorescence excitation in a p-terphenyl crystal. *Physical review letters* **65**, 2716 (1990).
- [18] Moerner, W. E. & Fromm, D. P. Methods of single-molecule fluorescence spectroscopy and microscopy. *Review of Scientific Instruments* **74**, 3597–3619 (2003).
- [19] Priest, L., Peters, J. S. & Kukura, P. Scattering-based light microscopy: from metal nanoparticles to single proteins. *Chemical reviews* **121**, 11937–11970 (2021).
- [20] Taylor, R. W. & Sandoghdar, V. Interferometric scattering microscopy: seeing single nanoparticles and molecules via rayleigh scattering. *Nano letters* **19**, 4827–4835 (2019).
- [21] Špačková, B. *et al.* Label-free nanofluidic scattering microscopy of size and mass of single diffusing molecules and nanoparticles. *Nature Methods* **19**, 751–758 (2022).
- [22] Stanciu, S. G. *et al.* Scattering-type scanning near-field optical microscopy of polymer-coated gold nanoparticles. *ACS omega* **7**, 11353–11362 (2022).
- [23] Devadas, M. S. *et al.* Detection of single gold nanoparticles using spatial modulation spectroscopy implemented with a galvo-scanning mirror system. *Applied Optics* **52**, 7806–7811 (2013).
- [24] Boyer, D., Tamarat, P., Maali, A., Lounis, B. & Orrit, M. Photothermal imaging of nanometer-sized metal particles among scatterers. *Science* **297**, 1160–1163 (2002).
- [25] Adhikari, S. *et al.* Photothermal microscopy: imaging the optical absorption of single nanoparticles and single molecules. *ACS nano* **14**, 16414–16445 (2020).

- [26] Asgari, N., Baaske, M. D., Ton, J. & Orrit, M. Exploring rotational diffusion with plasmonic coupling. *ACS photonics* (2024).
- [27] Zhu, J., Udupa, A. & Goddard, L. L. Visualizable detection of nanoscale objects using anti-symmetric excitation and non-resonance amplification. *Nature communications* **11**, 2754 (2020).
- [28] Zhuo, Y. *et al.* Single nanoparticle detection using photonic crystal enhanced microscopy. *Analyst* **139**, 1007–1015 (2014).
- [29] De Goede, M. *et al.* Al₂O₃ microring resonators for the detection of a cancer biomarker in undiluted urine. *Optics express* **27**, 18508–18521 (2019).
- [30] Tang, S.-J. *et al.* On-chip spiral waveguides for ultrasensitive and rapid detection of nanoscale objects. *Advanced Materials* **30**, 1800262 (2018).
- [31] Hendriks, A. L. *et al.* Detecting single nanoparticles using fiber-tip nanophotonics. *Optica* **11**, 512–518 (2024).
- [32] Su, J., Goldberg, A. F. & Stoltz, B. M. Label-free detection of single nanoparticles and biological molecules using microtoroid optical resonators. *Light: Science & Applications* **5**, e16001–e16001 (2016).
- [33] Fox, A. M. *Quantum optics: an introduction* Vol. 15 (Oxford University Press, USA, 2006).
- [34] Thompson, R., Rempe, G. & Kimble, H. Observation of normal-mode splitting for an atom in an optical cavity. *Physical review letters* **68**, 1132 (1992).
- [35] Hammerer, K. *et al.* Strong coupling of a mechanical oscillator and a single atom. *Physical review letters* **103**, 063005 (2009).
- [36] Groß, H., Hamm, J. M., Tufarelli, T., Hess, O. & Hecht, B. Near-field strong coupling of single quantum dots. *Science advances* **4**, eaar4906 (2018).
- [37] Hu, S. *et al.* Robust consistent single quantum dot strong coupling in plasmonic nanocavities. *Nature Communications* **15**, 6835 (2024).
- [38] Hennessy, K. *et al.* Quantum nature of a strongly coupled single quantum dot–cavity system. *Nature* **445**, 896–899 (2007).
- [39] Weisbuch, C., Nishioka, M., Ishikawa, A. & Arakawa, Y. Observation of the coupled exciton-photon mode splitting in a semiconductor quantum microcavity. *Physical review letters* **69**, 3314 (1992).
- [40] Qing, Y. M., Ren, Y., Lei, D., Ma, H. F. & Cui, T. J. Strong coupling in two-dimensional materials-based nanostructures: a review. *Journal of Optics* **24**, 024009 (2022).

- [41] Chikkaraddy, R. *et al.* Single-molecule strong coupling at room temperature in plasmonic nanocavities. *Nature* **535**, 127–130 (2016).
- [42] Liu, R. *et al.* Deterministic positioning and alignment of a single-molecule exciton in plasmonic nanodimer for strong coupling. *Nature Communications* **15**, 4103 (2024).
- [43] Lee, Y.-M., Kim, S.-E. & Park, J.-E. Strong coupling in plasmonic metal nanoparticles. *Nano Convergence* **10**, 34 (2023).
- [44] Maccaferri, N. *et al.* Recent advances in plasmonic nanocavities for single-molecule spectroscopy. *Nanoscale Advances* **3**, 633–642 (2021).
- [45] Shalabney, A. *et al.* Coherent coupling of molecular resonators with a microcavity mode. *Nature communications* **6**, 5981 (2015).
- [46] Dolado, I. *et al.* Remote near-field spectroscopy of vibrational strong coupling between organic molecules and phononic nanoresonators. *Nature Communications* **13**, 6850 (2022).
- [47] Simpkins, B. S., Dunkelberger, A. D. & Vurgaftman, I. Control, modulation, and analytical descriptions of vibrational strong coupling. *Chemical Reviews* **123**, 5020–5048 (2023).
- [48] De Abajo, F. G. & Howie, A. Retarded field calculation of electron energy loss in inhomogeneous dielectrics. *Physical Review B* **65**, 115418 (2002).
- [49] Hohenester, U. & Trügler, A. Mnpbem—a matlab toolbox for the simulation of plasmonic nanoparticles. *Computer Physics Communications* **183**, 370–381 (2012).
- [50] Hohenester, U. Simulating electron energy loss spectroscopy with the mnpbem toolbox. *Computer Physics Communications* **185**, 1177–1187 (2014).
- [51] Mortensen, N. A., Raza, S., Wubs, M., Søndergaard, T. & Bozhevolnyi, S. I. A generalized non-local optical response theory for plasmonic nanostructures. *Nature communications* **5**, 3809 (2014).
- [52] Scholl, J. A., Koh, A. L. & Dionne, J. A. Quantum plasmon resonances of individual metallic nanoparticles. *Nature* **483**, 421–427 (2012).
- [53] Maier, S. A. *et al.* *Plasmonics: fundamentals and applications* Vol. 1 (Springer, USA, 2007).
- [54] Luo, Y., Fernandez-Dominguez, A., Wiener, A., Maier, S. A. & Pendry, J. Surface plasmons and nonlocality: a simple model. *Physical review letters* **111**, 093901 (2013).

- [55] Garcia de Abajo, F. J. Nonlocal effects in the plasmons of strongly interacting nanoparticles, dimers, and waveguides. *The Journal of Physical Chemistry C* **112**, 17983–17987 (2008).
- [56] Tserkezis, C. *et al.* Hybridization of plasmonic antenna and cavity modes: Extreme optics of nanoparticle-on-mirror nanogaps. *Physical Review A* **92**, 053811 (2015).
- [57] Baumberg, J. J., Aizpurua, J., Mikkelsen, M. H. & Smith, D. R. Extreme nanophotonics from ultrathin metallic gaps. *Nature materials* **18**, 668–678 (2019).
- [58] Benz, F. *et al.* Sers of individual nanoparticles on a mirror: size does matter, but so does shape. *The journal of physical chemistry letters* **7**, 2264–2269 (2016).
- [59] Kongsuwan, N. *et al.* Plasmonic nanocavity modes: From near-field to far-field radiation. *ACS Photonics* **7**, 463–471 (2020).
- [60] Ojambati, O. S. *et al.* Efficient generation of two-photon excited phosphorescence from molecules in plasmonic nanocavities. *Nano Letters* **20**, 4653–4658 (2020).
- [61] Horton, M. J. *et al.* Nanoscopy through a plasmonic nanolens. *Proceedings of the National Academy of Sciences* **117**, 2275–2281 (2020).
- [62] Törmä, P. & Barnes, W. L. Strong coupling between surface plasmon polaritons and emitters: a review. *Reports on Progress in Physics* **78**, 013901 (2014).
- [63] Johnson, P. B. & Christy, R.-W. Optical constants of the noble metals. *Physical review B* **6**, 4370 (1972).
- [64] Elliott, E. *et al.* Fingerprinting the hidden facets of plasmonic nanocavities. *ACS photonics* **9**, 2643–2651 (2022).
- [65] Ruppin, R. Extinction properties of thin metallic nanowires. *Optics communications* **190**, 205–209 (2001).
- [66] Yang, Y. *et al.* A general theoretical and experimental framework for nanoscale electromagnetism. *Nature* **576**, 248–252 (2019).